Characteristics of Tropical Convective Gravity Waves Resolved by ERA5 Reanalysis

HAMID A. PAHLAVAN,[a] JOHN M. WALLACE,[a] AND QIANG FU[a]

[a] *Department of Atmospheric Sciences, University of Washington, Seattle, Washington*

(Manuscript received 8 March 2022, in final form 7 November 2022)

ABSTRACT: The ERA5 reanalysis with hourly time steps and ~30 km horizontal resolution resolves a substantially larger fraction of the gravity wave spectrum than its predecessors. Based on a representation of the two-sided zonal wavenumber–frequency spectrum, we show evidence of gravity wave signatures in a suite of atmospheric fields. Cross-spectrum analysis reveals (i) a substantial upward flux of geopotential for both eastward- and westward-propagating waves, (ii) an upward flux of westerly momentum in eastward-propagating waves and easterly momentum in westward-propagating waves, and (iii) anticyclonic rotation of the wind vector with time—all characteristics of vertically propagating gravity and inertio-gravity waves. Two-sided meridional wavenumber–frequency spectra, which are computed along individual meridians and then zonally averaged, exhibit characteristics similar to the spectra computed on latitude circles, indicating that these waves propagate in all directions. The three-dimensional structure of these waves is also documented in composites of the temperature field relative to grid-resolved, wave-induced downwelling events at individual reference grid points along the equator. It is shown that the waves radiate outward and upward relative to the respective reference grid points, and their amplitude decreases rapidly with time. Within the broad continuum of gravity wave phase speeds there are preferred values around ±49 and ±23 m s^{-1}, the former associated with the first baroclinic mode in which the vertical velocity perturbations are of the same sign throughout the depth of the troposphere, and the latter with the second mode in which they are of opposing polarity in the lower and upper troposphere.

KEYWORDS: Tropics; Gravity waves; Inertia-gravity waves; Reanalysis data; Atmospheric waves; Wave properties

1. Introduction

Gravity waves with a wide range of space and time scales are clearly discernible in the vertical velocity, horizontal wind, geopotential, and temperature fields in today's high-resolution global analyses. The upward transport of mechanical energy and momentum by gravity waves plays an important role in the dynamics of the middle atmosphere (Fritts and Alexander 2003).

Gravity waves can be excited by a variety of mechanisms including flow over topography, convection, shear instability, adjustment of unbalanced flow in the vicinity of jet streams and frontal systems, and wave–wave interactions (Fritts and Alexander 2003). The dissipation and breaking of convectively generated gravity waves have profound impacts on the dynamics of the tropical stratosphere. Together with planetary-scale Kelvin, mixed Rossby–gravity (MRG), and inertio-gravity (IG) waves, gravity waves are responsible for the descent of the alternating easterly and westerly wind regimes in the quasi-biennial oscillation (QBO) (Dunkerton 1997; Piani et al. 2000; Kawatani et al. 2010; Ern et al. 2014; Pahlavan et al. 2021b). They also contribute to modulating the tropopause temperature and the life cycle of cirrus clouds, both of which influence the water vapor transport to the stratosphere (Kim and Alexander 2015; Podglajen et al. 2016; Tseng and Fu 2017).

Our knowledge of gravity waves is limited due to their intermittency and small scales, and because motions on even smaller scales are involved in their generation and dissipation (Alexander et al. 2010; Geller et al. 2013). Numerous observational and modeling studies have been aimed at improving our knowledge and understanding of the waves excited by convection (e.g., Alexander et al. 1995; Piani et al. 2000; Lane et al. 2001; Song et al. 2003; Alexander et al. 2004). However, many of these investigations are focused on a single convective event and/or on a single observation site. Aircraft and balloons have been used to extend the subsynoptic-scale measurements over larger regions (e.g., Pautet et al. 2019; Rapp et al. 2021; Corcos et al. 2021), yet they can only provide local information on gravity wave characteristics. Satellite observations, while they reveal extensive wave structures (e.g., Alexander and Barnet 2007; Alexander and Ortland 2010; Ern et al. 2018; Wright et al. 2021), are also limited in their spatial and temporal coverage.

Despite the dramatic improvements in the computational power in the past decade, the spatial resolution of general circulation models has been too coarse (i.e., ~100 km) to properly resolve the smaller-scale gravity waves and to reveal their characteristics such as dissipation, interactions, spectral evolution, and source intermittency. Therefore, the effects of the unresolved gravity waves upon the global circulation are usually parameterized. These parameterization schemes, however, are oversimplified, leading to large uncertainties in the

Denotes content that is immediately available upon publication as open access.

Supplemental information related to this paper is available at the Journals Online website: https://doi.org/10.1175/JAS-D-22-0057.s1.

Corresponding author: Hamid A. Pahlavan, pahlavan@uw.edu

DOI: 10.1175/JAS-D-22-0057.1

atmospheric circulation characteristics (e.g., Garcia et al. 2017). In particular, simulation of the QBO remains challenging (Richter et al. 2020; Butchart et al. 2020; Bushell et al. 2022), and how the characteristics of the QBO might change in response to climate change is currently unclear. Very recently, global simulations at kilometer-scale resolutions have become feasible; however, they are still limited to relatively short simulations. Furthermore, these simulations are not constrained by observations, and are therefore subject to undocumented systematic errors.

The numerical weather prediction (NWP) models used in the production of global reanalyses have reached the horizontal resolution of 0.25° or less, which is sufficient to resolve waves with horizontal wavelengths of 300 km (e.g., Preusse et al. 2014; Jewtoukoff et al. 2015; Podglajen et al. 2020). Representation of the waves is improving not only because of increasing the model resolution, but also because of advances in data assimilation techniques and by the assimilation of an expanding array of data into the models. The gridded fields produced in the reanalyses are derived from NWP models constrained by observations, and as such, they could serve to bridge the gap between the sparse, spectrally limited observations from satellites and field campaigns and the unconstrained, short simulations with high-resolution models.

Several studies have examined the realism of the small-scale gravity waves in European Centre for Medium-Range Weather Forecasts (ECMWF) operational model (0.25° or 0.125° in the horizontal with 91 vertical levels) by comparing them with observations (Schroeder et al. 2009; Yamashita et al. 2010; Preusse et al. 2014; Jewtoukoff et al. 2015), and generally, have found them to be in good agreement. In this study, we use ERA5 (Hersbach et al. 2020), the newest reanalysis product of ECMWF's Integrated Forecasting System (IFS) to investigate the characteristics of gravity waves. With a spatial resolution of 0.28° (~31 km), and 137 hybrid model levels with a top at 0.01 hPa, ERA5 resolves a significant fraction of gravity wave spectrum. The unprecedented hourly temporal resolution in ERA5 also makes it possible to resolve waves with periods as short as 2 h.

Podglajen et al. (2020) investigated the gravity wave spectra in several of the reanalysis products using one-dimensional spectra in intrinsic-frequency space. They found that the reanalyses represent the spectral characteristics of the gravity waves quite realistically, notably the spectral gap between planetary and gravity waves in the frequency domain. They also documented the intermittency properties and probability density function of gravity wave field and showed that they are consistent with long-duration, quasi-Lagrangian balloon observations. Among the various reanalyses that they examined, they found ERA5 to be most realistic.

Gupta et al. (2021) used ERA5 to investigate the role of gravity waves during the Antarctic polar vortex breakdown. They showed that the resolved wave forcing in ERA5 accounts for as much as one-fourth of the observed wind deceleration during the period of the breakdown. In an intercomparison between five different reanalyses, they also showed that wave-induced drag in ERA5 is by far the strongest.

Pahlavan et al. (2021a) investigated the momentum budget of the QBO in ERA5. They showed that half of the required QBO wave forcing is provided by resolved waves, approximately twice as much as in ERA-Interim, the previous reanalysis product from ECMWF (Dee et al. 2011), with horizontal resolution of 0.75° and 60° vertical levels. They also showed that this difference is mainly attributable to forcing from small-scale gravity waves with wavelengths shorter than 2000 km, which do not make an important contribution in ERA-Interim (their Fig. 14).

Hoffmann and Spang (2022) compared the tropopause characteristic between ERA5 and ERA-Interim and found that ERA5 shows significantly more variability in the tropopause heights and temperatures, which is attributed to the larger fraction of the gravity wave spectrum being resolved in ERA5.

The purpose of this study is to investigate the characteristics of the resolved, convectively generated gravity waves in ERA5 over the tropics. Figure 1 provides an example of these short-wavelength, high-frequency gravity waves. The top panel is a visible image in the Pacific Ocean obtained by the *Himawari-8* satellite, which shows several synoptic-scale systems with embedded deep convection at 0200 UTC 7 August 2015. Figure 1b shows the field of vertical velocity at the 50 hPa level from ERA5 for the same time and region. The black contours denote the 250 K brightness temperature from *Himawari-8* and are indicative of thick clouds with cold tops. The 50 hPa level is well above the top of these clouds, so the vertical velocity perturbations at this level are produced mainly by vertically propagating gravity waves. Several concentric arrays of waves are radiating outward from the center of the convective systems, with the wave fronts wrapped in tight spirals: a pattern that has been observed in satellite images, observations, and numerical simulations (e.g., Nolan and Zhang 2017). The propagation of the waves is mostly eastward, which is expected, given that the zonal wind background was easterly, at around 15 m s^{-1} at the 50 hPa level at that time. Figure 1c shows the standard deviation of the field of vertical velocity at the 50 hPa level for the 24-h period centered on 0200 UTC on this day. The enhanced variance around and to the east of the convective systems is clear and is indicative of enhanced wave activity.

In this study, we further examine the representation of these tropical convectively induced gravity waves in ERA5. We first introduce a representation of the two-sided zonal wavenumber–frequency spectrum that is well suited for the study of tropical gravity waves. This representation is then used to examine the spectral characteristics of gravity waves. We show that a suite of atmospheric fields exhibits clear gravity wave signatures. The three-dimensional structure and evolution of the waves is further analyzed by means of compositing analysis. Our results show that data from ERA5 can provide valuable information on gravity wave spectral characteristics, structure, and propagation, and thereby help to fill a key knowledge gap that underlies the current deficiencies in weather and climate modeling.

The paper is organized as follows. A description of ERA5 dataset and our methodology is given in section 2, and we present and discuss the results in sections 3 and 4: in section 3a

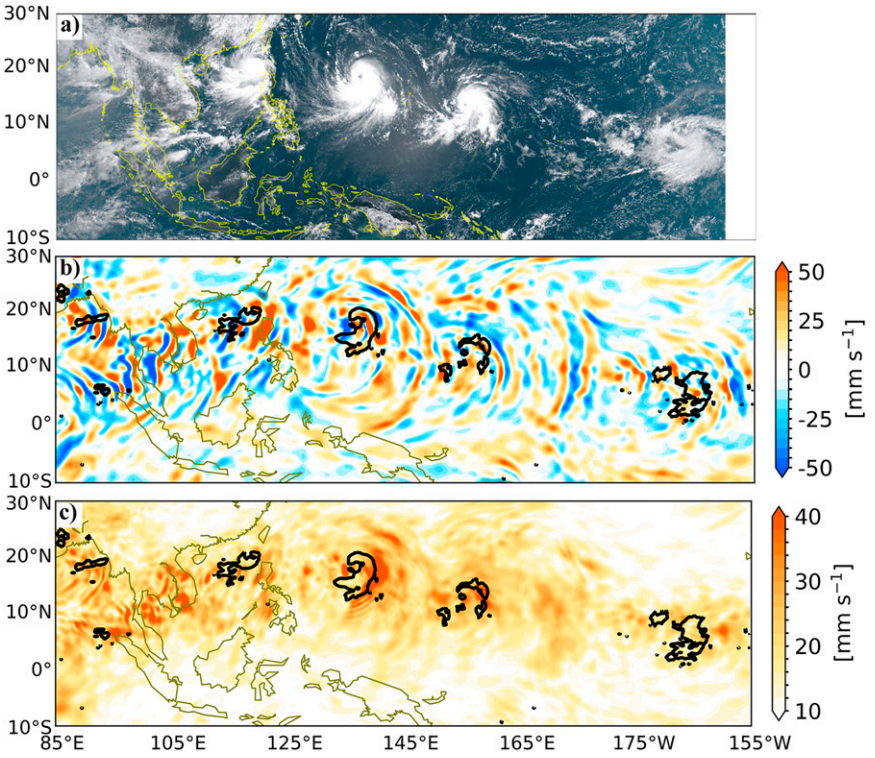

FIG. 1. (a) Visible imagery of the tropical Pacific Ocean from the *Himawari-8* satellite at 0200 UTC 7 Aug 2015. (b) Vertical velocity at the 50 hPa level from ERA5 for the same time and region (colored shading). (c) Standard deviation of the field of vertical velocity at the 50 hPa level for the 24-h period centered on 0200 UTC on this day (colored shading). The black contours in (b) and (c) denote the 250 K brightness temperature from *Himawari-8* and are indicators of thick clouds with cold tops.

the results of spectrum and cross-spectrum analysis relating to waves with a broad continuum of phase speeds and in section 3b results of compositing analysis that document the structure and evolution of the waves. Section 4 shows observational evidence of preferred modes of variability based on normalized cross-spectra between fluctuations in geopotential at different levels. Concluding remarks are presented in section 5.

2. Data and methodology

The ERA5 data are the fifth generation of ECMWF reanalysis products, which is produced using the IFS cycle 41r2 with four-dimensional variational (4DVar) data assimilation. Two artificial sponge layers are used in IFS to damp wave motions that disperse upward to avoid wave reflections at the model top (Shepherd et al. 2018). A weak sponge that starts at the 10 hPa level, and a stronger sponge that starts at the 1 hPa level.

ERA5 has 0.28° horizontal resolution, 137 vertical levels, and hourly available data. Its predecessor, ERA-Interim, had 0.75° horizontal resolution, 60 vertical levels, and 6-hourly time steps. These improvements allow for a better representation of high-frequency and/or small-scale gravity waves that are known to be sensitive to resolution (Hoffmann et al. 2019; Hersbach et al. 2020). Furthermore, the use of an updated and significantly improved NWP model and data assimilation system compared to the earlier reanalyses, along with the incorporation of data from additional sources, have improved the prediction skill of the forecast model used in producing ERA5, making it possible to use a smaller data assimilation increment (Hoffmann et al. 2019).

In this study, we retrieve ERA5 hourly data at 0.25° × 0.25° horizontal sampling on standard pressure levels. Most of the results shown in this paper are based on a 10-yr period (2010–19) of hourly data. Examples will be shown, which confirm that very similar results are obtained when the same analyses are performed on 41 years of data (1979–2019).

Though the dynamical core can, in principle, resolve waves with a horizontal wavelength twice the horizontal resolution, hyperdiffusion, which is introduced to provide numerical stability, limits the wavelengths of well-resolved waves to about 10 spatial grid points, or even coarser (Skamarock et al. 2014; Preusse et al. 2014). Considering the horizontal resolution of 31 km of ERA5 (639 spectral coefficients), we can expect that waves with horizontal wavelengths longer than ~400 km (zonal wavenumber $k < 100$) to be well resolved. Shorter waves are present, but they are suppressed in amplitude (see Fig. 7a of Stephan and Mariaccia 2021).

Many of the results presented in this paper are based on spectral analysis in which the variance of a variable $A(x, t)$ on a latitude circle, where x is the zonal coordinate and t is time, is transformed into a two-sided power spectrum $P_A(k, \omega)$, where k is zonal wavenumber and ω is frequency. The power spectrum is the product of the space–time discrete Fourier transform of the variable, $F_A(k, \omega)$ with its complex conjugate $F_A^*(k, \omega)$:

$$P_A(k, \omega) = F_A(k, \omega) F_A^*(k, \omega). \quad (1)$$

The cross-spectrum between A and B is given by the product of the Fourier transform of A and the complex conjugate of the Fourier transform of B:

$$P_{AB}(k, \omega) = F_A(k, \omega) F_B^*(k, \omega). \quad (2)$$

The real part of P_{AB} is referred to as the *cospectrum* (Co) and the imaginary part is called the *quadrature spectrum* (Q). The sum of cospectral estimates over all wavenumbers and frequencies is equal to the covariance between A and B. The quadrature spectrum can be considered as the cospectrum between A and B, where the phase of B is 90° shifted for a given frequency and wavenumber. We also make use of the *coherence spectrum* (Coh), which is defined as

$$\mathrm{Coh}(k, \omega) = \left(\frac{\mathrm{Co}^2 + Q^2}{P_A P_B} \right)^{0.5} \quad (3)$$

as well as the *normalized* cospectrum and quadrature spectrum: i.e., Co and Q divided by $(P_A P_B)^{0.5}$. Coherence is a standardized measure of the strength of the linear relationship between the fluctuations in two variables that applies regardless of the phase difference between them. Finally, the *phase spectrum* (Ø) can be defined as

$$\text{Ø}(k, \omega) = \tan^{-1} \frac{Q}{\mathrm{Co}}, \quad (4)$$

which can be interpreted as the phase difference between A and B that yields the greatest coherence for any zonal wavenumber and frequency, positive if fluctuations in A lead those in B.

To calculate the spectral coefficients, we first subdivide the 10-yr hourly time series (2010–19) into segments with the length of 48 days, overlapping by 35 days, which results in ~280 time segments on each latitude circle. The length of the segments (i.e., 48 days) is chosen such that waves with periods as long as 10 days are well resolved. From each segment, the linear trend is removed, and the time series segments are tapered with the Hann window, which goes to zero at the edges. Then, a two-dimensional Fourier transform is applied to each time segment over latitude circles ranging from 30°S to 30°N at 1° intervals (i.e., 61 latitude circles), which results in a total of ~17 000 spectra (i.e., 280 × 61).

We then average all the spectra, after weighting each by the cosine of latitude to account for the reduction of the areas of the grid cells away from the equator. This averaging over time segments and latitude circles smooths the final spectrum. A similar averaging procedure is employed for the cross-spectral analysis, after calculating the cross-spectrum on each latitude circle for each time segment. The coherence and phase spectra are then calculated from the final smooth spectra.

3. Results

a. Spectral analysis

Matsuno (1966) derived and solved a system of dry shallow-water equations on an equatorial beta plane, linearized with respect to a resting basic state. These solutions are often displayed in terms of what is called a dispersion diagram, which has been extensively used to study the zonally propagating planetary-scale waves in the tropics. In this paper, we make some modifications to the traditional diagram, which makes it more appropriate to study the small-scale gravity waves (Fig. 2). To span the wide range of frequencies and wavenumbers resolved by ERA5, we use logarithmic scales for both horizontal and vertical coordinates, which correspond to zonal wavenumber (k) and frequency (ω), respectively. The right side (positive k) corresponds to eastward-propagating waves, and the left side (negative k) corresponds to westward-propagating waves. The curves represent the spectral signatures of equatorial Kelvin waves, MRG waves, and eastward- and westward-propagating IG waves and gravity waves. In this paper, we use the term IG for referring to the low-frequency gravity waves for which the rotation of Earth has an important influence. The curves for the IG waves asymptote rather rapidly to the respective gravity wave curves at higher frequencies. It is evident that tropical waves with frequencies higher than 1 cycle per day and/or wavenumbers larger than 20 are predominantly gravity (as opposed to IG) waves. Equatorial Rossby waves do not appear in this plot because their frequencies are lower than 0.1 cycles per day. In this logarithmic representation, nondispersive waves such as Kelvin and gravity waves, for which ω/k is constant, appear as straight lines with a slope of one decade increase of ω per decade increase of $|k|$. Differences in phase speed are reflected, not as differences in slope, but as vertical displacements of the phase speed line. The black curves in both Figs. 2a and 2b are for an equivalent depth (h_e) of 54 m, which corresponds to a phase speed (c) of 23 m s^{-1} for gravity waves (i.e., $c = \sqrt{gh_e}$). The gray curves in Fig. 2b are for a phase speed of 49 m s^{-1}. These phase speeds match the features in the spectra shown next. We use this modified version of the Matsuno's dispersion diagram to investigate the spectral characteristics of gravity waves in ERA5.

1) Zonal wavenumber–frequency spectra

Figure 3 shows the power spectrum of surface pressure, which is shown first because it is better constrained by observations than the other fields. While most radiosonde data are available only twice per day, ERA5 assimilates hourly observations of surface fields from ~5000 aviation meteorology support (METAR) stations throughout the world as well as surface observations from another 10 000 synoptic meteorological

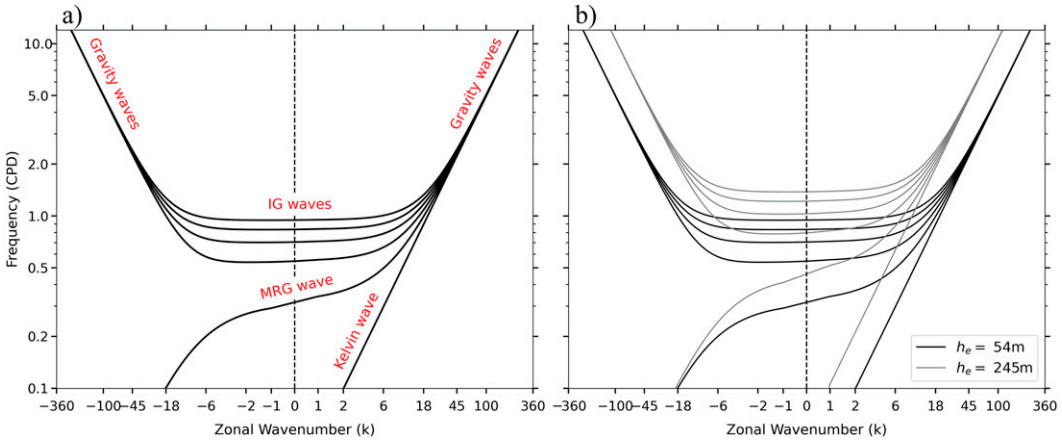

FIG. 2. (a) Dispersion diagram for a system of dry shallow-water equations on an equatorial beta plane, with an equivalent depth (h_e) of 54 m to match a phase speed (c) of 23 m s^{-1} for gravity waves (i.e., $c = \sqrt{gh_e}$), plotted on logarithmic scales for both zonal wavenumber and frequency coordinates. The highest frequency in the spectra is 12 cycles per day (cpd), which is the Nyquist frequency (highest resolvable frequency) when hourly data are used. The zonal wavenumber is linear in the range $k = -1$ to 1. (b) The black curves are as in (a), but the gray curves are for an equivalent depth of 245 m to match a phase speed of 49 m s^{-1}.

(SYNOPS) stations that report four times per day or more frequently (Haiden et al. 2018).

Note that a logarithmic scale is also used for indicating the spectral power (or density) in the observed spectra, which spans through several orders of magnitude. The spectral power is multiplied by $k \times \omega$ to preserve the property that (power × area) be proportional to variance anywhere on the plot. For clarity, instead of displaying the whole set of dispersion curves as in Fig. 2, only the two lines of constant slope corresponding to the gravity waves with phase speeds of ±23 and ±49 m s^{-1} are plotted for reference.

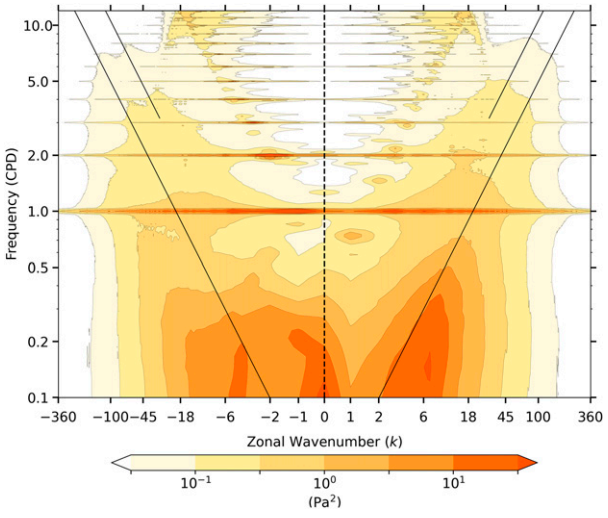

FIG. 3. Two-sided zonal wavenumber–frequency power spectrum for surface pressure on a logarithmic scale for wavenumber, frequency, and spectral density in unit of variance per unit area, from an average of spectra computed at 1° latitude intervals between 30°S and 30°N based on hourly data for 2010–19. The spectral power is multiplied by $k \times \omega$ to preserve the property that (power × area) be proportional to variance anywhere on the plot. The contour interval corresponds roughly to a factor of 3. The sloping straight black lines correspond to phase speeds of ±49 m s^{-1} (upper) and ±23 m s^{-1} (lower). The scale of zonal wavenumber is linear from $k = -1$ to 1.

The power spectrum of surface pressure (Fig. 3) exhibits a set of very thin horizontal bands centered on the diurnal period and its higher harmonics corresponds to the astronomically forced solar (24-h and its higher harmonics) and lunar (12.4-h) tides. Because of the geographically fixed boundary-forced component of the tides, peaks are observed on both sides of the spectrum, rather than only on the westward-propagating side. The additional isolated peaks for each zonal wavenumber correspond to the external modes of the global atmosphere, which are extensively analyzed by Sakazaki and Hamilton (2020).

The focus of the present study is the internal gravity waves, which extend along the broad swaths in the wavenumber–frequency domain for both eastward- and westward-propagating waves. The spectrum is continuous and spans a broad range of phase speeds, but there is evidence of two slightly preferred phase speeds, a faster one around ±49 m s^{-1}, and a slower one around ±23 m s^{-1}. We will show in section 4 that these correspond to internal waves with stratospheric vertical wavelengths of about 14 and 6.5 km, respectively.

Figure 4 shows the zonal wavenumber–frequency power spectra of zonal (u), meridional (v), and vertical (w) wind components, and temperature (T) at the 50 hPa level, constructed in the same manner as Fig. 3. The broad swaths related to the gravity waves are evident in all of them, including the evidence of two slightly preferred phase speeds, the same as in Fig. 3. Most of the variance of the temperature and horizontal wind fields is concentrated in the low frequencies and small

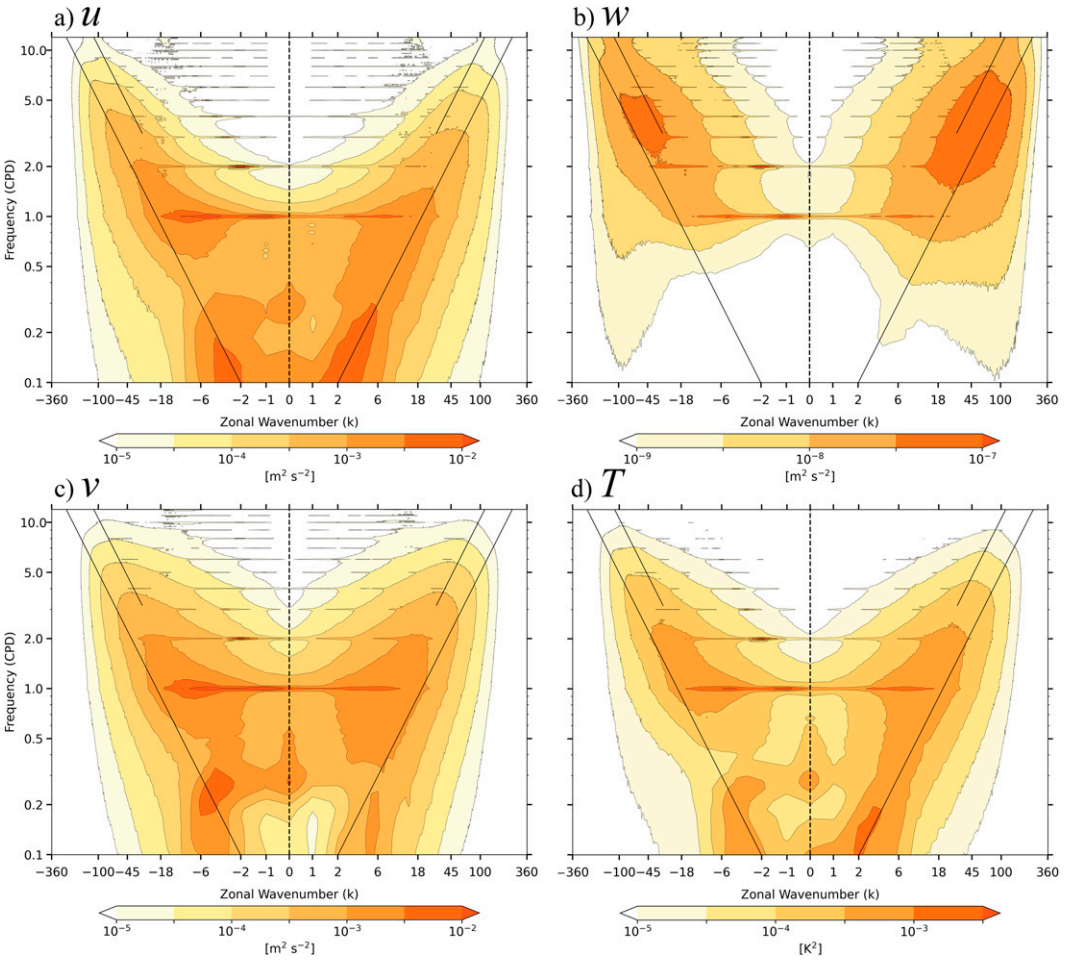

FIG. 4. As in Fig. 3, but for (a) zonal wind, (b) vertical velocity, (c) meridional wind, and (d) temperature at the 50 hPa level.

wavenumbers, whereas most of the variance of the vertical wind component is concentrated at the higher frequencies.

The zonal wavenumber–frequency power spectrum of vertical wind constructed using 41 years (1979–2019) of hourly data (Fig. S1 in the online supplemental material) is very similar to Fig. 4b, which is based on 10 years of data (2010–19). Hence, for the sake of computational efficiency, the shorter period has been used for performing analysis in this study.

The background flow in the stratosphere is often varying on a time scale much longer than the period of the gravity waves, and hence, the linear theory is useful for describing the spectral characteristics of the waves in the stratosphere (Fritts and Alexander 2003). In the troposphere the separation between time scales is not as clean and the presence of convection and turbulence makes it more difficult to separate the gravity waves from the noisy background.

To evaluate the consistency of the observed spectra with linear gravity wave theory, we now examine the relations between different variables. Cross-spectra for selected variables at the 50 hPa level are shown in Fig. 5. The cospectrum between w and geopotential (Φ), an indicator of the vertical flux of geopotential and mechanical energy, is shown in Fig. 5a. It is upward for both eastward- and westward-propagating waves, consistent with theory. The upward flux of zonal momentum (Fig. 5b) is positive for eastward-propagating waves and negative for westward-propagating waves, also consistent with theory. Figure 5b also shows that the flux of eastward momentum is upward for MRG waves, which will be discussed in more detail later. The quadrature spectrum between T and Φ (Fig. 5c) is much stronger than the corresponding cospectrum (Fig. S2), which indicates that T and Φ are nearly in quadrature. The positive sign of the quadrature spectrum also indicates that variations of T precedes the variations of Φ (i.e., T leads Φ), which is indicative of downward phase propagation. These relationships are characteristic of upward-dispersing internal gravity waves.

In the quadrature spectrum between the poleward meridional wind component v_p (i.e., v in the Northern Hemisphere and $-v$ in the Southern Hemisphere) and zonal wind (Fig. 5d),

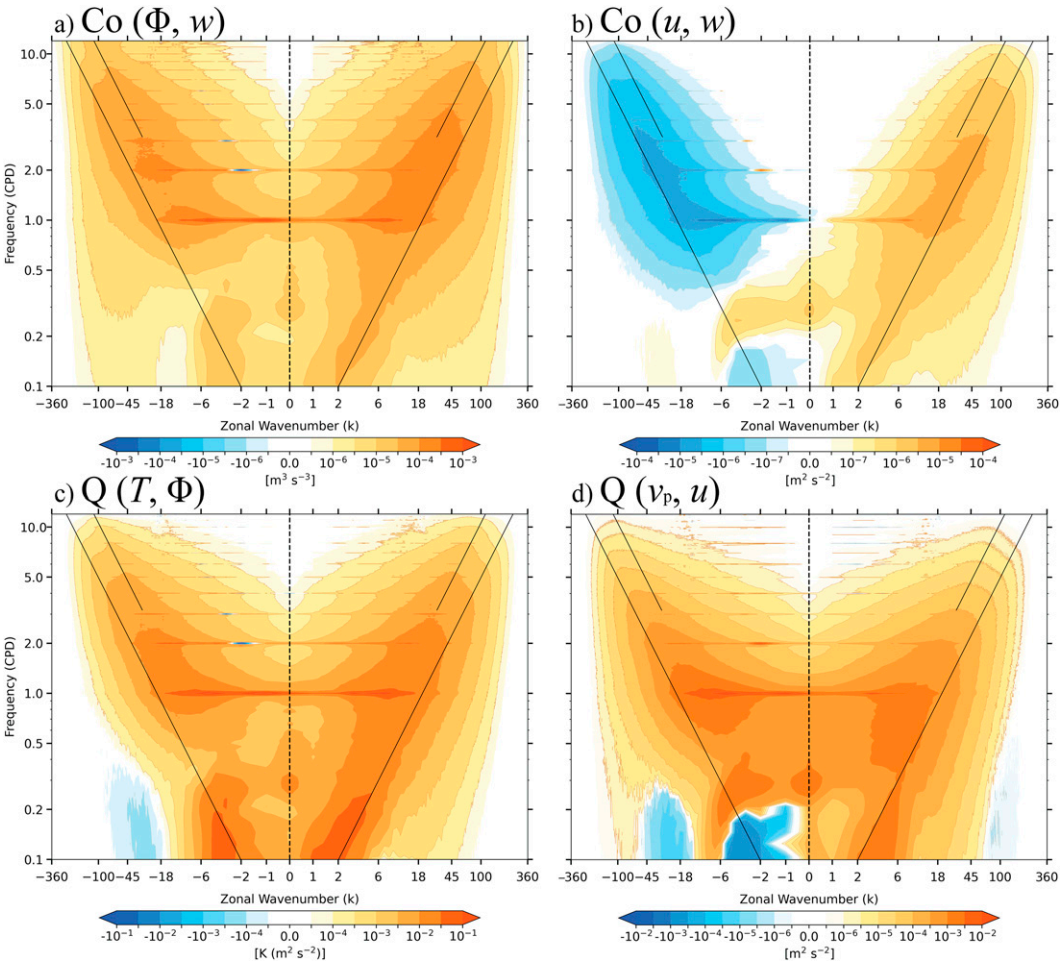

FIG. 5. As in Fig. 3, but for the cospectrum (Co) between (a) geopotential and vertical velocity and (b) zonal wind and vertical velocity, and the quadrature spectrum (Q) between (c) temperature and geopotential and (d) poleward meridional wind (i.e., northward in the Northern Hemisphere and southward in the Southern Hemisphere) and zonal wind. All fields are at the 50 hPa level.

v_p leads u for both eastward- and westward-propagating waves, indicative of clockwise rotating trajectories of wind vectors in the hodograph with time in the Northern Hemisphere and counterclockwise rotating trajectories in the Southern Hemisphere—i.e., an anticyclonic turning of the wind vector with time in their respective hemispheres. The prevalence of anticyclonic rotation of the wind vectors is indicative of the presence of IG waves: no systematic phase relation between the horizontal wind components is observed in stratified turbulence. The relationships between other variables, which are not shown here, are also consistent with the structure of vertically propagating IG waves. For example, temperature is in quadrature with vertical velocity, while in quasigeostrophic turbulence they are either in phase or out of the phase by 180°. About half the vertical flux of zonal momentum shown in Fig. 5b is attributable to fluctuations with zonal wavenumbers higher than 20 and periods shorter than one day, which also attests to the importance of gravity waves in the general circulation of the tropical stratosphere.

Another notable feature in Fig. 5 is the MRG wave, which is evident in all the plots and particularly in Fig. 5b, where it is seen to transports westerly momentum upward. However, as explained in Holton (1973), the mean meridional circulation associated with MRG waves leads to a net upward transfer of easterly absolute angular momentum. Evidence of this transport can be seen in Fig. 13 of Pahlavan et al. (2021b). The blue patches at frequencies less than 0.2 cpd and wavenumbers $k = -1$ to -6 in Figs. 5b and 5d are related to extratropical Rossby waves, which propagate into the tropical stratosphere from the winter hemisphere. Another low-frequency blue patch is discernible in Figs. 5c and 5d at wavenumbers $k \approx -18$ to -45. This signal, which is present only during the easterly phase of the QBO (not shown), seems to be related to slowly eastward-propagating

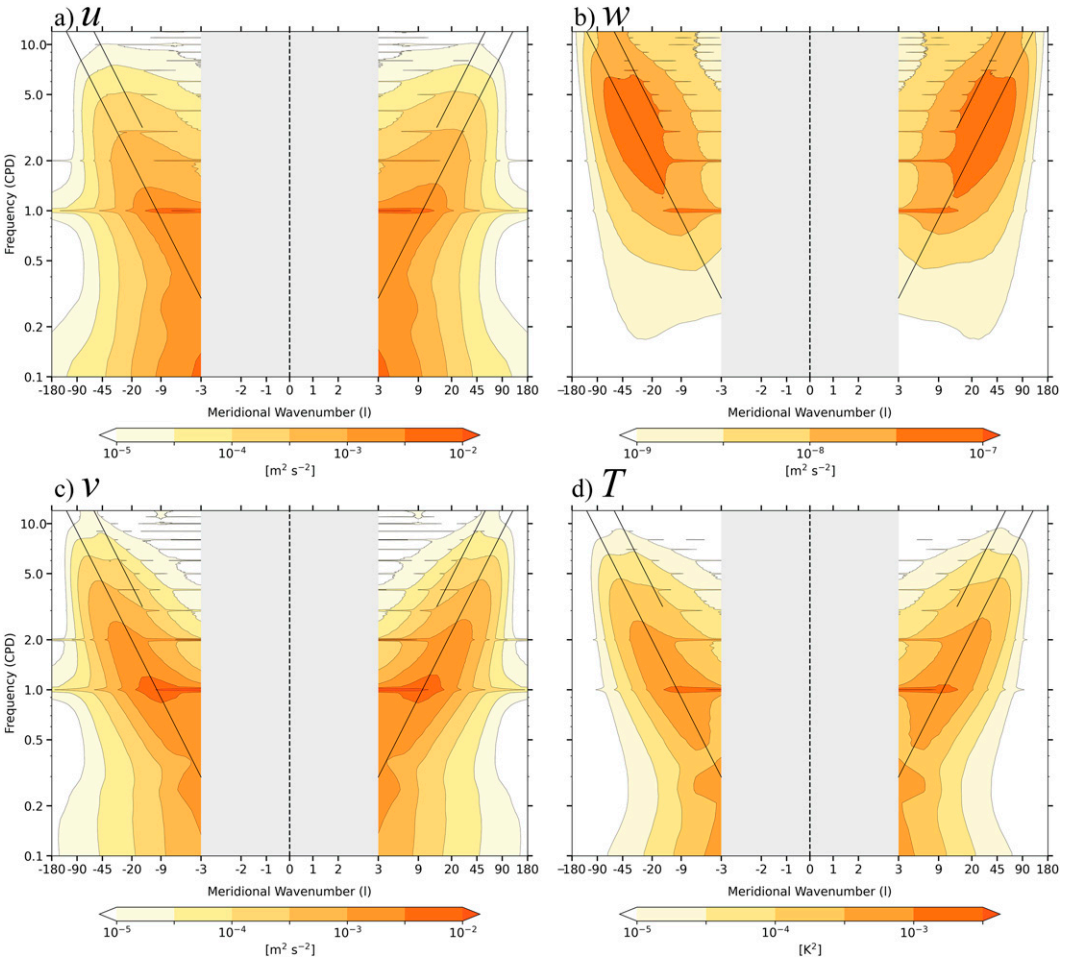

FIG. 6. Two-sided meridional wavenumber–frequency spectrum for (a) zonal wind, (b) vertical velocity, (c) meridional wind, and (d) temperature at the 50 hPa level. It is constructed in the same manner as Fig. 4, but the two-dimensional Fourier transform is applied along each meridian from 30°S to 30°N at 2° zonal intervals (i.e., along 180 meridians). Because only a 60° span of latitude is used in computing the spectra, meridional wavenumber 3 is the longest wave that can be sampled. The sloping straight black lines correspond to phase speeds of ±49 m s^{-1} (upper) and ±23 m s^{-1} (lower). The scale of meridional wavenumber is linear from $l = -1$ to 1.

waves that are advected westward during these intervals. This feature will be discussed in more detail in a paper currently in preparation.

2) MERIDIONAL WAVENUMBER–FREQUENCY SPECTRA

In contrast to equatorially trapped planetary-scale waves, which propagate only zonally, small-scale, high-frequency gravity waves are expected to propagate radially away from their sources, as seen in Fig. 1, and consequently, to exhibit similar spectral characteristics along any arbitrarily chosen direction. To test this, we repeated our spectral analysis, this time performing a two-dimensional Fourier transform along each meridian from 30°S to 30°N at 2° zonal intervals (i.e., along 180 meridians).

The results are shown in Figs. 6 and 7. Here the horizontal coordinate is a function of meridional wavenumber (l), rather than zonal wavenumber (k): the right side (positive l) represents northward- (rather than eastward-) propagating, and the left side (negative l) represents southward- (rather than westward-) propagating waves. Because only a 60° span of latitude is used in computing the spectra, meridional wavenumber 3 is the longest wave that can be sampled. It should be noted that meridional wavenumber 180 has the same horizontal scale as zonal wavenumber 360: they both are representative of waves with a wavelength of 1°.

The two-sided meridional wavenumber–frequency power spectra presented in Fig. 6 exhibit the same characteristics as those shown in Fig. 4, including the same two slightly preferred phase speeds, confirming that both the slightly preferred waves and the waves in the background continuum propagate in all directions, as expected for gravity waves. For all variables, the spectra are almost perfectly symmetric about $l = 0$ due to the absence of a strong background meridional

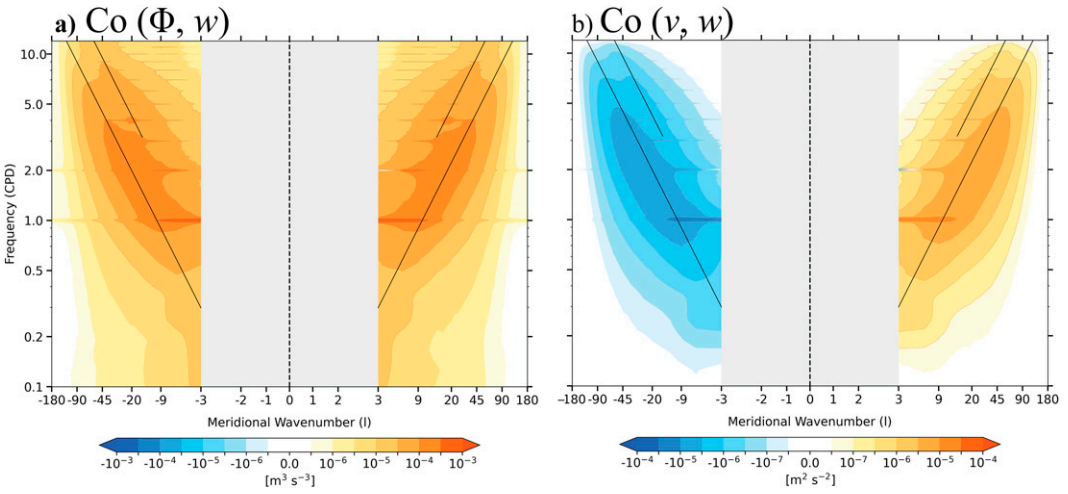

FIG. 7. As in Fig. 6, but for the cospectrum (Co) between (a) geopotential and vertical velocity and (b) meridional wind and vertical velocity. All fields are at the 50 hPa level.

wind. It follows that their net wave forcing on the background meridional flow should be close to zero.

Figure 7 shows the relations between the different variables along the meridional direction. Figure 7a is indicative of an upward flux of geopotential, consistent with the structure of vertically propagating gravity waves, and analogous to that in Fig. 5a. The vertical flux of meridional momentum (Fig. 7b) is indicative of an upward flux of northward momentum by northward-propagating waves and an upward flux of southward momentum by southward-propagating waves.

Figure S3 shows the same cospectra as in Figs. 5b and 7b, but with the contours of the normalized cospectrum superimposed. Within the loops enclosed by these contours, which include the abovementioned broad swaths, upward-dispersing gravity waves are the dominant form of variability.

In the meridional-wavenumber spectrum, the shape of the power spectrum of meridional wind (Fig. 6c), is analogous to that of zonal wind in the zonal-wavenumber spectrum (Fig. 4a). Likewise, the shape of the power spectrum of zonal wind in the meridional-wavenumber spectrum (Fig. 6a), is analogous to that of meridional wind in the zonal-wavenumber spectrum (Fig. 4c). Hence, to compare the two, it is useful to refer to the wind components parallel to and perpendicular to the axis used in defining the wavenumber coordinate. In both Fig. 4 and Fig. 6, at frequencies higher than 1 cpd, the preference for phase speeds higher than $\sim$49 m s^{-1} is stronger in the component perpendicular to the axis than in the component parallel to the axis. This feature is best illustrated in Fig. 8, which shows the ratio of the spectra of the horizontal winds in both zonal- and meridional-wavenumber spectra. The blue-shaded region between the $\pm$49 m s^{-1} phase speed lines with $\omega > 1$ cpd is characterized

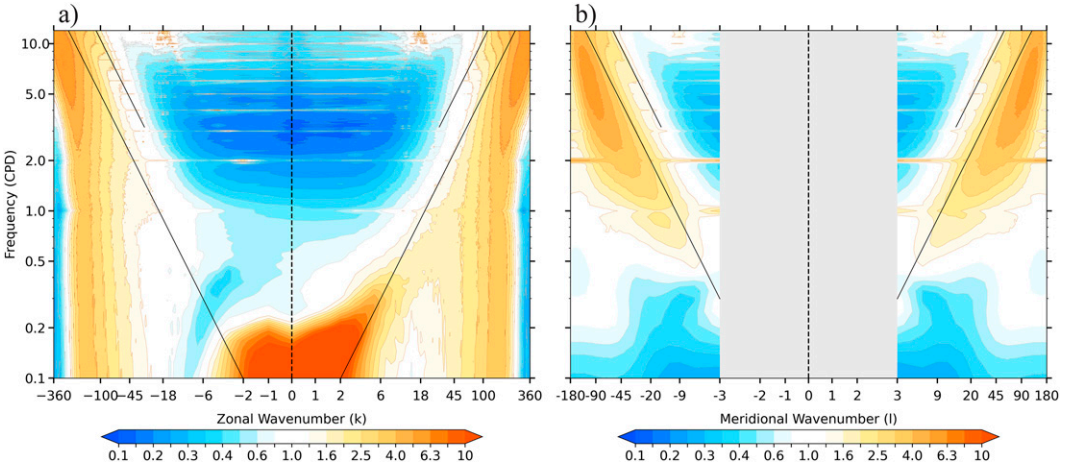

FIG. 8. (a) Two-sided zonal wavenumber–frequency spectrum for the ratio of zonal wind power spectrum to the meridional wind power spectrum [i.e., $P_u(k, \omega)/P_v(k, \omega)$] in a logarithmic scale. (b) Two-sided meridional wavenumber–frequency spectrum for the ratio of meridional wind to zonal wind power spectra [i.e., $P_v(l, \omega)/P_u(l, \omega)$].

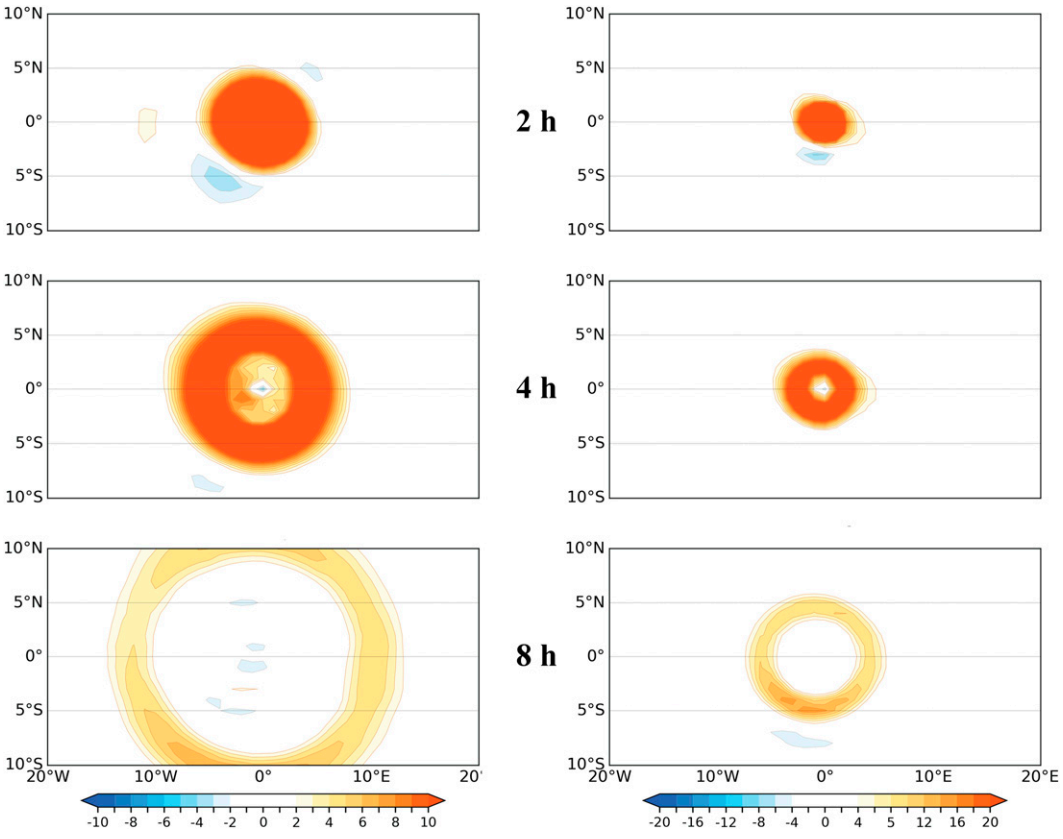

FIG. 9. Composites of high-pass filtered tropical tropospheric temperature constructed based on the top 10% of strongest downwelling events at individual referenced grid points along the equator, shown (top) 2, (middle) 4, and (bottom) 8 h after the events, using hourly data for 2010–19. (left) The reference time series is the sum of standardized 700 and 300 hPa vertical velocities, and the temperature field is calculated based on geopotential height difference between the 1000 and 200 hPa levels. (right) The reference time series is the difference of standardized 300 and 700 hPa vertical velocities, and the temperature field is calculated based on the difference of geopotential height between the 500 and 200 hPa levels. Units are arbitrary.

by stronger power in the wind component perpendicular to the axis; i.e., the waves tend to be meridionally elongated in the zonal wind field and zonally elongated in the meridional wind field. An explanation of this pronounced anisotropy is beyond the scope of the present study.

b. *Compositing analysis*

In this subsection, we investigate the three-dimensional structure of the small-scale gravity waves by compositing different variables based on time series of tropospheric vertical velocity at individual grid points equally spaced along the equator at 1° intervals (i.e., 360 grid points). After constructing the composites at individual grid points, they are all moved to a reference grid point (here 0° longitude) and averaged together. Hence, the longitude coordinate in the composites panels is only relative and does not imply the geographical location.

The left panels in Fig. 9 show maps of mean tropospheric temperature composited based on wave-induced downwelling events. The downwelling events are defined by the sum of standardized 700 and 300 hPa vertical velocities ($w_{700} + w_{300}$), which closely resembles the principal component of the leading mode of variability of the vertical profile of vertical velocity in the tropical troposphere. To qualify as a wave-induced downwelling event, an hourly observation of ($w_{700} + w_{300}$) must lie in the bottom 10% of its frequency distribution at that grid point.

The mean tropospheric temperature is calculated based on geopotential height difference between the 1000 and 200 hPa levels using the hypsometric equation [see Eq. (3.29) of Wallace and Hobbs 2006]. Strictly speaking, this quantity is mean virtual temperature. The mean for each hour of the day has been removed from the geopotential height field in order to suppress the tidal signal. The data have been also high-pass filtered[1] in order to isolate the signature of high-frequency gravity waves, which is much weaker than the

[1] The high-pass filtering was performed by applying a rolling window of 7-point binomial distribution [i.e., (−1, −6, −15, 44, −15, −6, −1)] to the time series at each individual grid point.

temperature variability on longer time scales. The absolute amplitude of the composited variable is dependent on the filtering protocol and is thus of no interest in its own right: it is the patterns that we are interested in.

The right panels of Fig. 9 are different from the left panels in two respects: they show the *upper-tropospheric* temperature, computed as the difference of geopotential height between the 500 and 200 hPa levels, and they are based on the *difference* between standardized 300 and 700 hPa vertical velocities ($w_{300} - w_{700}$), which resembles the second principal component of the vertical velocity profile. The fields shown in the left column thus correspond to relatively deep waves in which vertical velocity perturbations of the same polarity extends through the depth of the troposphere, whereas those in the right panel correspond to shallower waves that undergo a phase reversal in the midtroposphere.[2]

The patterns revealed by these composites are of extremely high statistical significance as evidenced by the well-defined shapes of the rings radiating out from the reference grid point and the absence of features elsewhere in the plots. The remarkably high signal to noise ratio is due to the large number of degrees of freedom inherent in the hourly data. The compositing analysis is based on 10 years of hourly data. Hence, at each of the 360 grid points there are (365×24) events, yielding a total of roughly 3 million downwelling events ($360 \times 365 \times 24$). Some of these events are probably overlapping and are not entirely independent from each other. However, the temporal autocorrelation of vertical velocity at individual grid points is weak and drops below ~0.4 after only 2 h. The correlation between the vertical velocity time series at grids with degree longitude apart along the equator is also weak (also ~0.4).

A very conservative estimate of the number of degrees of freedom is ~300 000, when only 10% of the events are considered to be statistically independent, which results to the Z scores represented in Fig. S4, and indicates that the signal is still statistically significant at the 10^{-15} level 8 h after the reference time.

The horizontal cross sections in Fig. 9 reveal an almost radially symmetric structure at all levels. The waves radiate outward from the reference grid point. The deeper wave propagates at about twice the rate of the shallower one, with a phase speed of ~50 versus ~25 m s^{-1}, consistent with the two preferred phase speeds seen in the spectra shown in the previous section. Further evidence of the existence of two (albeit slightly) preferred modes, widely referred to by Haertel and Kiladis (2004) and others as "the first and second baroclinic modes" is presented in section 4. The expanding rings are a signature of adiabatically induced subsidence warming in downwelling gravity waves. The waves spread the latent heat injected into the atmosphere in convective updrafts into the large-scale environment (Bretherton and Smolarkiewicz 1989), thereby imposing weak-temperature gradient (WTG) balance between the vertical velocity and diabatic heating fields throughout most of the tropical troposphere.

There exist numerous observations of gravity waves in the upper atmosphere, which are generated by convective sources and are rendered recognizable by virtue of their concentric or semiconcentric patterns in ground-based and satellite imagery (e.g., Miller et al. 2015). For example, Dewan et al. (1998) analyzed gravity waves in the satellite observations from the Midcourse Space Experiment. The density and temperature fluctuations, which were measured at an altitude of ~40 km, showed wave fronts organized in concentric circles centered over a large thunderstorm. There are also numerous satellite images and videos from the Hunga Tonga eruption on 15 January 2022, which show concentric internal and external waves radiating outward after the eruption. Recently, Wright et al. (2022) documented the broad spectrum of waves that was triggered by this eruption using a comprehensive set of satellite and ground-based observations. Furthermore, there are several modeling studies of the structure of convectively generated gravity waves in the tropics that show wave fronts radiating out from centers of strong diabatic heating (e.g., Piani et al. 2000).

In our composites, reference grid points act as receivers as well as a transmitters of gravity waves. Strong downwelling events occur when the downwelling phase of the waves coming from all directions arrives at the reference grid point at the same time (time zero in the composites). Hence, almost a perfect symmetry of the patterns can be seen with respect to lag time as shown in Fig. 10. Since the vertical velocity and temperature perturbations in gravity waves occur in quadrature with one another, the strongest downwelling corresponds to the largest time rate of change of temperature, both of which occur at time zero. The lowest temperature at the reference grid point is observed an hour earlier and the highest temperature an hour later. It should be emphasized that the patterns in our composites show the propagation of downwelling gravity waves, but they do not reveal the processes that generated them, which occur on scales much smaller than the ERA5 horizontal resolution of ~30 km.

The expanding ring in the right panels of Fig. 10 retains its identity and continues to propagate radially outward at an almost constant rate of about 1.5° of latitude per hour (close to 49 m s^{-1}) out to a lag of at least 16 h, as shown in Fig. S5, and Table 1. As the ring expands it weakens until the pattern eventually begins to become noisier. The scaled root-mean-squared (rms) amplitude, indicated by the numerical value in the upper-left corner of each panel, decreases monotonically as its radius increases. The squared amplitude times the area of the ring declines as well, as can be inferred from Table 1. These weakening, yet highly coherent rings represent only a small fraction of the variance associated with gravity waves. It is apparent from the spectra that most of the variance is associated with waves with a broad continuum of phase speeds, which undergo strong cancellation in the composites for the longer lag times, leaving only the nondispersive waves whose narrow spectral peaks stand out above the background continuum.

[2] Results similar to Fig. 9 are also obtained by performing principal component analysis (PCA) on the vertical velocity profiles and regressing the temperature field upon the expansion coefficients of the first and second modes.

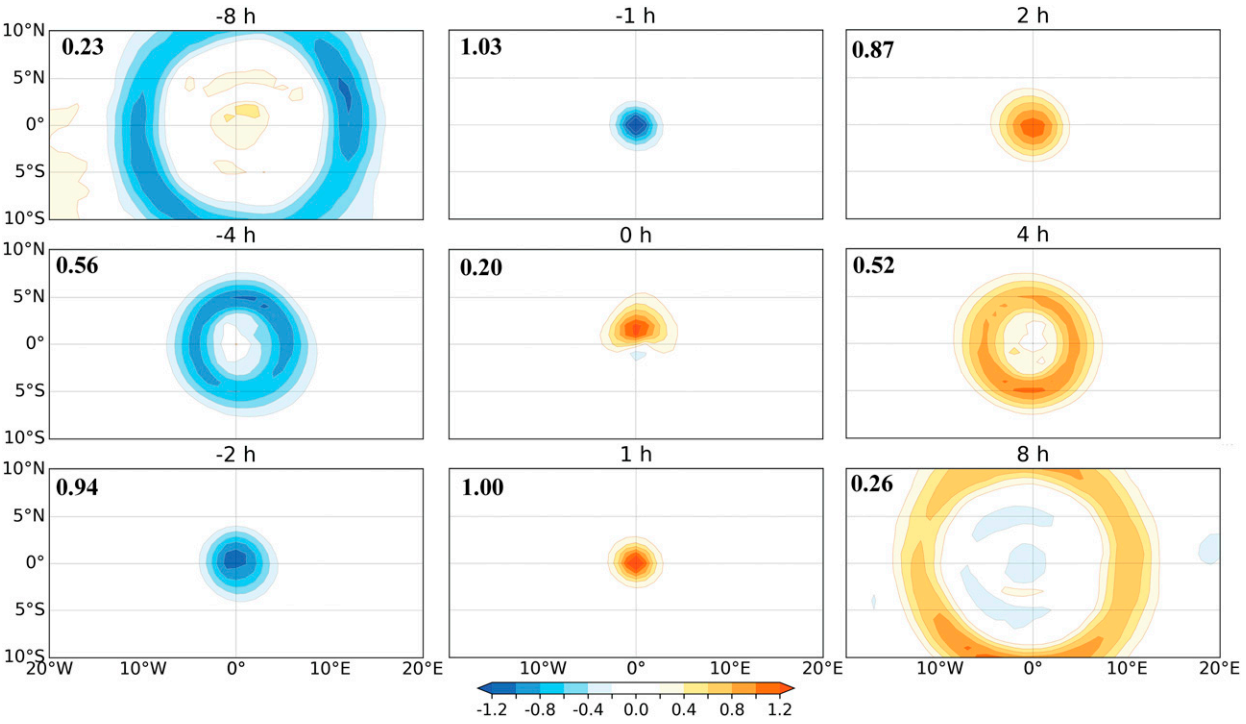

FIG. 10. (right) As in the left panel of Fig. 9, except the plotted values in each panel are normalized relative to the average magnitude of the 1% of grid points with the strongest signal. (left),(center) Composites at the other time lags as indicated. The numbers in the top-left corner of each panel are root-mean-squared (rms) amplitude, calculated based on the grid points in the domain 30°S–°N, 30°W–°E and normalized with respect to its value at 1 h lag.

Figure 11 shows horizontal maps at the 50 hPa level (left), and the equatorial longitude–height sections (right) of temperature, composited based on the gravest mode, as represented by the sum of w_{300} and w_{700}. The wave fronts radiate outward and upward relative to the respective reference grid points, and their amplitude decreases rapidly with time. The zonal cross sections show how gravity waves are refracted as they disperse upward from the troposphere into the stratosphere, due to the change in static stability at the tropopause, with the phase fronts assuming a V-shaped configuration (Lane et al. 2001). Upon close inspection, it is evident from the zonal cross sections that the wave axes are propagating downward in the stratosphere, while the group velocity and the vertical flux of mechanical energy is upward and outward. The zonal cross sections of temperature composited based on the second mode (i.e., $w_{300} - w_{700}$) are shown in Fig. S6. It is more difficult to capture the signal of the second mode based on compositing or regression analysis.

Figure 12 shows the corresponding structure in the wave-related fields in the three velocity components and geopotential at the 50 hPa level for the first mode, 8 h after the strong downwelling events. It is evident that geopotential, vertical velocity, and the radial wind component all vary in phase with each other, indicative of an upward flux of radial momentum and mechanical energy, consistent with the results of spectral analysis. There is also a weak suggestion of an anticyclonic rotation of the horizontal wind vector, as expected in IG waves.

It can be seen from Figs. 9–11 that the convectively generated gravity waves modify the troposphere by inducing adiabatic warming and cooling, and therefore, we might expect to see their signals in the other fields as well, as shown in Fig. S7, which is constructed in the same manner as bottom-left panel of Fig. 9. Figure S7 shows the gravity wave signatures in the cloud cover fraction, outgoing longwave radiation (OLR), and precipitation, and thus, documents the importance of gravity waves in modifying the state of the troposphere in

TABLE 1. Summary of the scaled variance (i.e., mean squared amplitude) of the composites shown in Fig. 10 calculated in the same manner as the rms amplitude printed in Fig. 10 but not square rooted. The *radius* is the distance between the reference grid point and strongest part of the ring directly to the south of it. *Mean squared amplitude* or variance is calculated based on the grid points in the domain 30°S–°N, 30°W–°E and is scaled based on its amplitude at 1-h lag.

Time lag (h)	Radius (degress of latitude)	Scaled mean squared amplitude
1	—	1.000
2	2	0.757
4	5	0.275
8	11	0.067
12	17	0.025
16	23	0.017

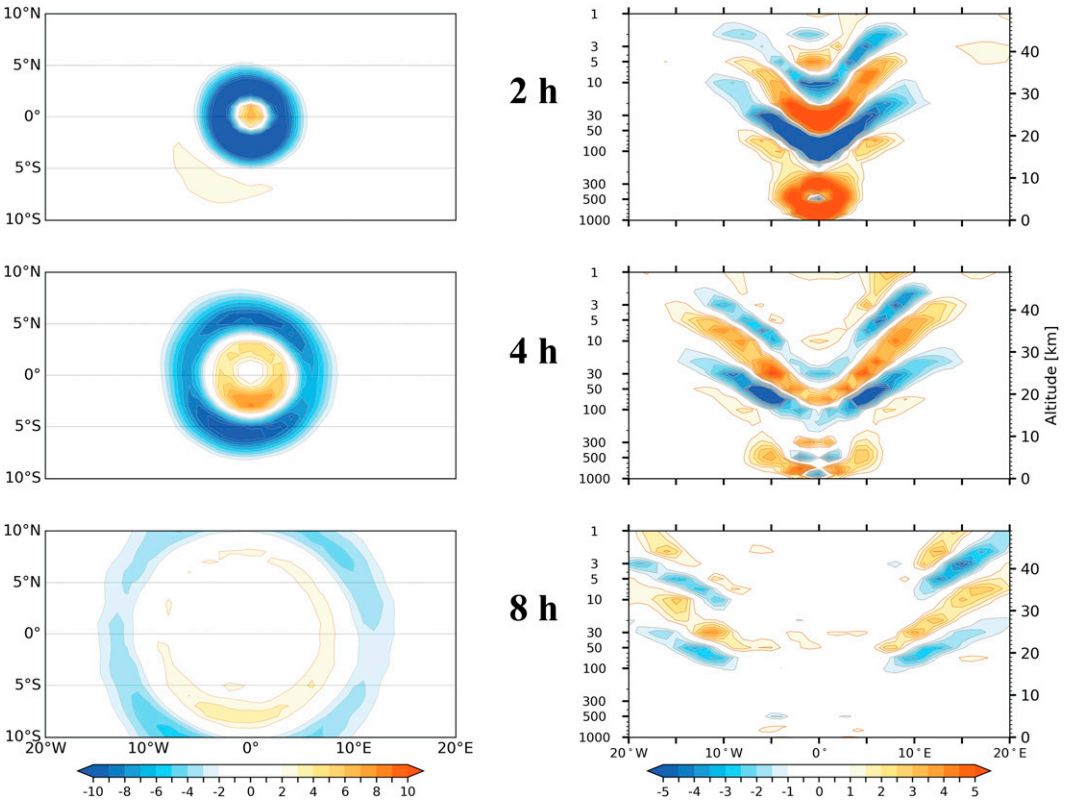

FIG. 11. Composites of high-pass filtered tropical temperature constructed based on the top 10% of strongest downwelling events at individual referenced grid points along the equator, shown (top) 2, (middle) 4, and (bottom) 8 h after the events, using hourly data for 2010–19. The reference time series is the sum of standardized 700 and 300 hPa vertical velocities. (left) Horizontal cross sections of temperature at the 50 hPa level. (right) The corresponding longitude–height cross sections of temperature along the equator. Units are arbitrary.

addition to transporting energy and momentum upward into the stratosphere. It is noted from Fig. S7 that these fields are not exactly in phase (or out of phase).

In the horizontal sections shown in Figs. 9–12, the meridional phase propagation is slightly stronger than the zonal propagation. A possible cause of this departure from circular symmetry is the greater variability of the zonal wind variations in the background flow, due in large part to the QBO in the stratosphere and the Madden–Julian oscillation (MJO) in the troposphere. Another contributing factor could be the fact that the patches of enhanced convection from which the waves emanate tend to be zonally elongated.

c. *Seasonal dependence of gravity waves propagation*

The composites shown in Fig. 13 are constructed in the same manner as those in the bottom-left panel of Fig. 9, but separately for the 3-month seasons. It is readily apparent that the prevailing direction of wave propagation is northward in DJF and southward in JJA. The radial symmetry is greater during the transition seasons, yet a slight preference for northward propagation is evident during MAM and for southward propagation during SON. These asymmetries in the direction of wave propagation relate to the distribution of wave sources relative to the reference grid points, which are located along the equator. At times when the prevailing component of the propagation is southward, as in JJA, we can infer that the wave sources should be located mainly to the north of the equator, and vice versa.

This is indeed the case, as shown in Fig. 14, which shows the standard deviation of the unfiltered hourly pressure velocity field at the 50 hPa level, an indicator of wave activity. From this figure it can be inferred that the dominant regions of tropical wave activity correspond to the regions of strong convection, which are mostly located to the south of the equator during DJF and to the north of the equator during JJA. Tropical wave activity is significantly stronger during JJA than DJF (Fig. 14), and the southward component of wave propagation is more prevalent (Fig. 13). Other notable features in Fig. 14 are the higher latitude, orographically induced waves and the enhanced wave activity along the extratropical storm tracks.

4. Observational evidence of preferred phase speeds

Waves generated by convective heating are widely believed to have vertical wavelengths approximately twice the depth of

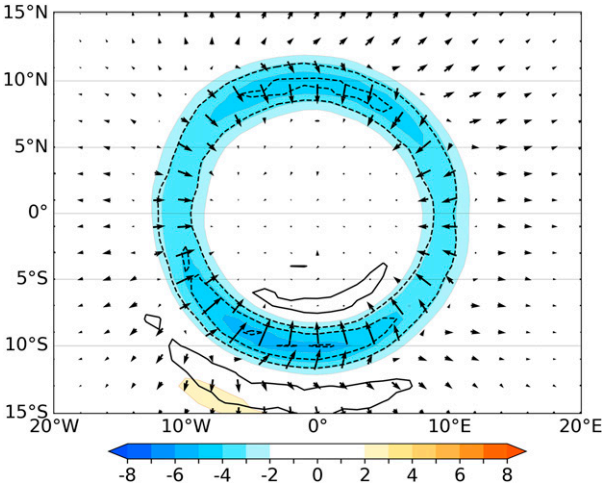

FIG. 12. Composite of high-pass filtered geopotential (colored shading), vertical velocity (positive upward, zero contour omitted, negative contours dashed), and horizontal winds (vectors) at the 50 hPa level based on top 10% of strongest downwelling events at individual reference grid points along the equator, shown 8 h after the reference time. The reference time series is the sum of standardized 700 and 300 hPa vertical velocities. Units are arbitrary.

the heating. This relationship, demonstrated by Garcia and Salby (1987) for large-scale waves, arises because the heating projects most strongly onto a wave with a vertical wavelength twice the depth of the heating. As the waves disperse upward from the troposphere into the stratosphere, they are refracted, and their vertical wavelength decreases to half its tropospheric value due to the twofold increase in buoyancy frequency at the tropopause. The frequency, and the horizontal, and vertical wavelengths of waves are then mutually related through the wave dispersion relationship. A simplified version of the dispersion relation for medium-frequency gravity waves can be written as (Fritts and Alexander 2003)

$$\hat{c}_p = \frac{N\lambda_z}{2\pi}, \tag{5}$$

where $\hat{c}_p$ is the intrinsic phase speed, λ_z the vertical wavelength, and N the Brunt–Väisälä frequency, which is usually prescribed to be 0.022 s^{-1} at the stratospheric levels. Based on this equation, the stratospheric vertical wavelength for waves with intrinsic phase speeds of 49 and 23 m s^{-1} should be ~14 and ~6.5 km. Hence, we can expect that they should be generated by convective heating with depths of ~14 and ~6.5 km, respectively.

These wavelengths are consistent with the vertical scale of the first and second modes of the vertical profile of vertical velocity. Through the buoyancy force, the latent heating and vertical motion in the tropical troposphere are intrinsically coupled. It is also consistent with the vertical structure of the waves obtained by compositing analysis shown in Fig. 11 and Fig. S6. Based on the EOF analysis of the tropical vertical velocity profiles, the first mode, which is associated with the heating profile in deep convection, explains about half of the variance and the second mode, associated with stratiform precipitation, explains another 20%.[3]

The dominance of the leading EOFs of the vertical velocity field suggests there should exist preferred modes of convective forcing, which would lead to the preferred vertical wavelengths and phase speeds. Observational confirmation of the existence of two preferred modes is provided by Fig. 15, which shows the normalized zonal wavenumber–frequency cospectrum and quadrature spectrum between geopotential field at the 1000 and 200 hPa levels in the 10°S–10°N latitude belt. The black curve represents the dispersion relationship for an IG wave with zero meridional mode (i.e., $n = 0$) in a resting atmosphere (see Fig. 2), and the red curve is for an atmosphere with an easterly background flow of 3 m s^{-1}, which is closer to the observed annual mean, vertically averaged zonal flow in this belt.

Note the prominent band along the 49 m s^{-1} phase speed line in the left panel. That it is negative (blue) indicates that the faster mode tends to be out of phase at these two levels and thus manifests its signature in 1000–200 hPa thickness, an indicator of tropospheric temperature, the variable for the left panels of Fig. 9. The signal of the slower mode along the 23 m s^{-1} phase speed line is weaker, but nonetheless highly statistically significant,[4] and it is also evident in a quadrature spectrum, shown in the right panel. These internal gravity wave signatures are to be distinguished from the discrete positive (orange) spectral peaks associated with the much more rapidly propagating external modes discussed by Sakazaki and Hamilton (2020).

Our results confirm the existence of preferred first and second baroclinic modes, consistent with the literature, but we also see a continuum of gravity waves with a broad range of phase speeds. The existence of the continuum is further illustrated by spectral analysis between geopotential at the 10 and 50 hPa levels, shown in Fig. 16. These two levels are 11 km apart. Only the part of the spectrum with $\omega > 0.5$ cpd and $l > 3$ is shown. At any frequency, the waves that exhibit peaks in the quadrature spectrum at vertical wavelength λ are the ones for which $(n/2 + 0.25)\lambda = 11$, where $n = 1, 2, \ldots$. The odd integers correspond to negative peaks and the even numbers to positive ones. This relationship yields 14.6, 8.8, 6.2, 4.8, 4 km for the vertical wavelengths, which [via Eq. (5)] corresponds to phase speeds of 51, 31, 22, 17, and 14 m s^{-1}, respectively. The banded structure in the quadrature spectrum is in accord with this relationship and an analogous

[3] It should be noted that relating the vertical wavelength of the gravity waves only to the vertical structure of the diabatic forcing might not be appropriate (Lane and Moncrieff 2008). Holton et al. (2002) argue that for diabatic forcing of a given frequency, gravity waves will have vertical wavelengths of about twice the depth of the heating only when the ratio of vertical-to-horizontal scale of the heating is compatible with the vertical-to-horizontal wavenumber ratio given by the dispersion relationship.

[4] A conservative estimate of the degree of freedom is 1000, for which a value of 0.1 at this spectrum is significant at the 0.01 level.

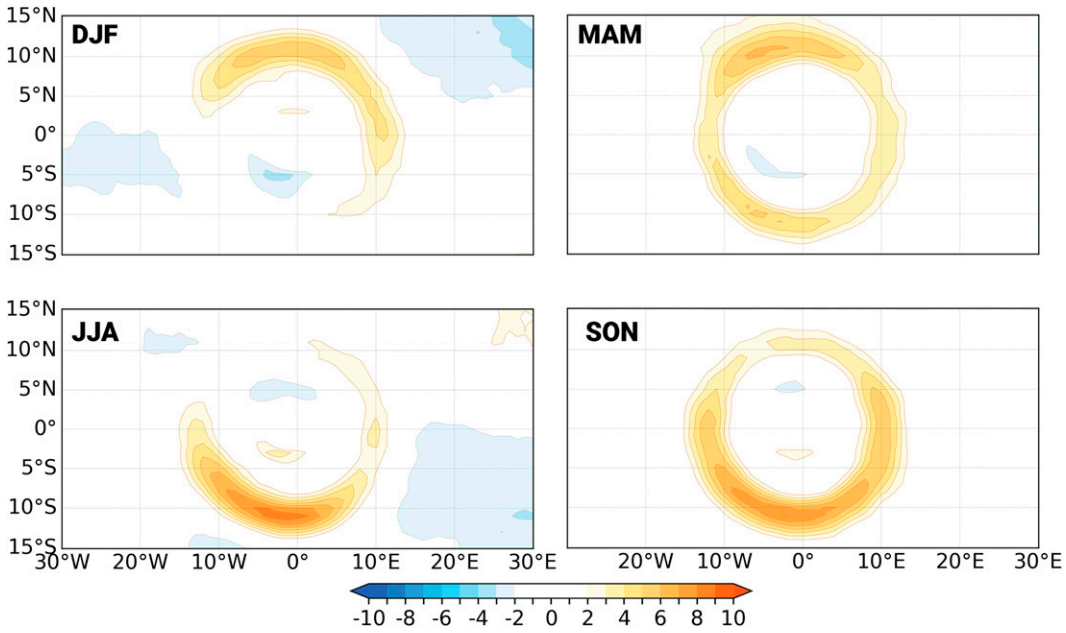

FIG. 13. As in the bottom-left panel of Fig. 9, but separated for four seasons.

relationship are observed in the cospectrum (Fig. 16a) and the phase spectrum (Fig. 16d). It is notable that this structure is a property of the continuum of phase speeds: it exists independently of any preferred modes that might be superimposed upon it. However, consistent with Fig. 15, the coherence spectrum (Fig. 16c) is strongest in the vicinity of the 51 m s^{-1} phase speed line.

5. Discussion and concluding remarks

The compositing results presented in Figs. 9–13 are constructed based on downwelling events. Figure S8, which was constructed in the same manner as the left panels of Fig. 9, shows the corresponding patterns for upwelling events. The waves are of reversed polarity and only about half as strong as those associated with the downwelling events, even though

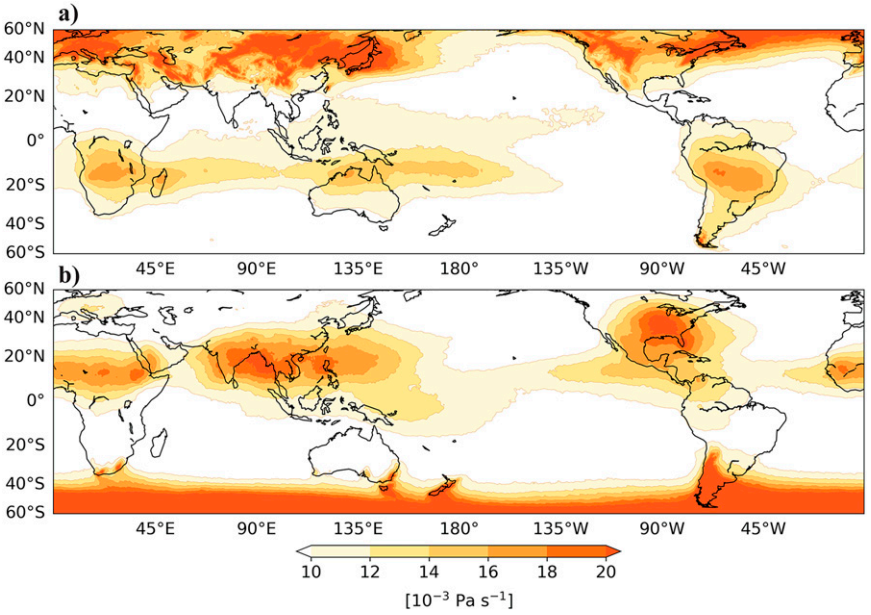

FIG. 14. Climatology of the standard deviation of pressure velocity at the 50 hPa level for (a) DJF and (b) JJA, based on hourly data for 2010–19.

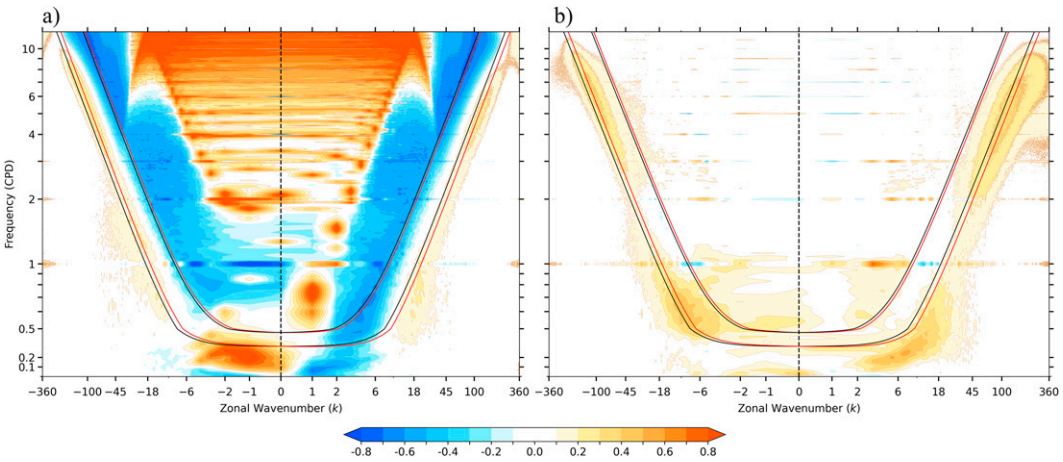

FIG. 15. The normalized two-sided zonal wavenumber–frequency (a) cospectrum and (b) quadrature spectrum between perturbations in the geopotential field at the 1000 and 200 hPa levels computed at 1° latitude intervals between 10°S and 10°N based on hourly data for 2010–19. The black curve represents the dispersion relationship for an IG wave with zero meridional mode (i.e., $n = 0$) in a resting atmosphere, and the red curve is for an atmosphere with an easterly background flow of 3 m s^{-1}, as observed. The scale of zonal wavenumber is linear from $k = -1$ to 1, and the scale of frequency is linear from $\omega = 0$ to 0.5. The reflection of the signal of external modes at higher frequencies in the cospectrum is due to aliasing and implies the presence of waves with frequencies higher than 12 cpd that are undersampled with an hourly sampling.

the events that triggered them (i.e., the vertical velocity perturbations at time zero) are about 1.6 times as strong in absolute value. A possible explanation for this disparity is that there is some cancellation between the adiabatic cooling in wave-induced upwelling events and diabatic heating due to the release of latent heat in deep convection. Since the deep convection is mostly unresolved in ERA5, the wave-induced adiabatic cooling dominates, resulting in an anomalously colder temperature. Based on the results presented in Haertel and Kiladis (2004), if convection and its associated diabatic heating were fully resolved in ERA5, the degree of cancellation would be around 95% for the first mode, resulting in an even weaker temperature signature for the upwelling events.

In this paper, we have investigated the characteristics of convectively generated gravity waves in the tropics using the ERA5 dataset, and provided unique information on their spectrum, structure, and propagation in the atmosphere. Two-sided spectra and cross-spectra for a suite of atmospheric fields at the 50 hPa level, shown in section 3a, exhibit a continuum of phase speeds. Superimposed upon this continuum is a slight enhancement of the variance within narrow bands centered on phase speeds around ±49 and ±23 m s^{-1}, which correspond to the first and second baroclinic modes of the vertical profile of diabatic heating. The broader continuum is not clearly apparent in studies in which the spectra are computed using the methodology described in Wheeler and Kiladis (1999), because a smooth background spectrum is subtracted out. Compositing analysis presented in section 3b reveals the three-dimensional structure of the waves with preferred phase speeds as manifested in various atmospheric fields. Further observational evidence of the existence of these two modes is presented in section 4.

In this study, the gravity wave spectra and compositing results relating to the waves at the stratospheric levels are based on a 10-yr period (2010–19), which includes both westerly and easterly phases of the QBO. The dependence of the properties of gravity waves upon the phase of the QBO is under investigation.

The ability of the ERA5 to resolve much of the broad spectrum of gravity waves opens avenues for further explorations in wave-driven variability of the general circulation. For instance, it provides a basis for investigating the wave-driven variability of the QBO period and amplitude, a topic that has previously been investigated only based in models. In section 3c, we only briefly discussed the seasonality of the tropical wave activity. The strongest wave activity during JJA is north of 10°N (Fig. 15), which is too far poleward to directly affect the QBO near the equator. How this spatiotemporal variability of wave activity modulates the stratospheric circulation, including the characteristics of the QBO can be studied using ERA5. It also provides a basis for investigating how the other dominant modes of the tropical variability including El Niño–Southern Oscillation (ENSO), and MJO modulate the tropical wave activity and thereby influence the stratospheric circulation.

In all the reanalysis products, including ERA5 (and even in the models with resolutions much higher than ERA5), a significant part of the variability is still missing, especially at high frequencies and/or on short wavelengths, and hence needs to be parameterized. In the future, improved vertical and horizontal resolutions, and data assimilation strategies will enable NWP models to resolve an increased fraction of wave-induced

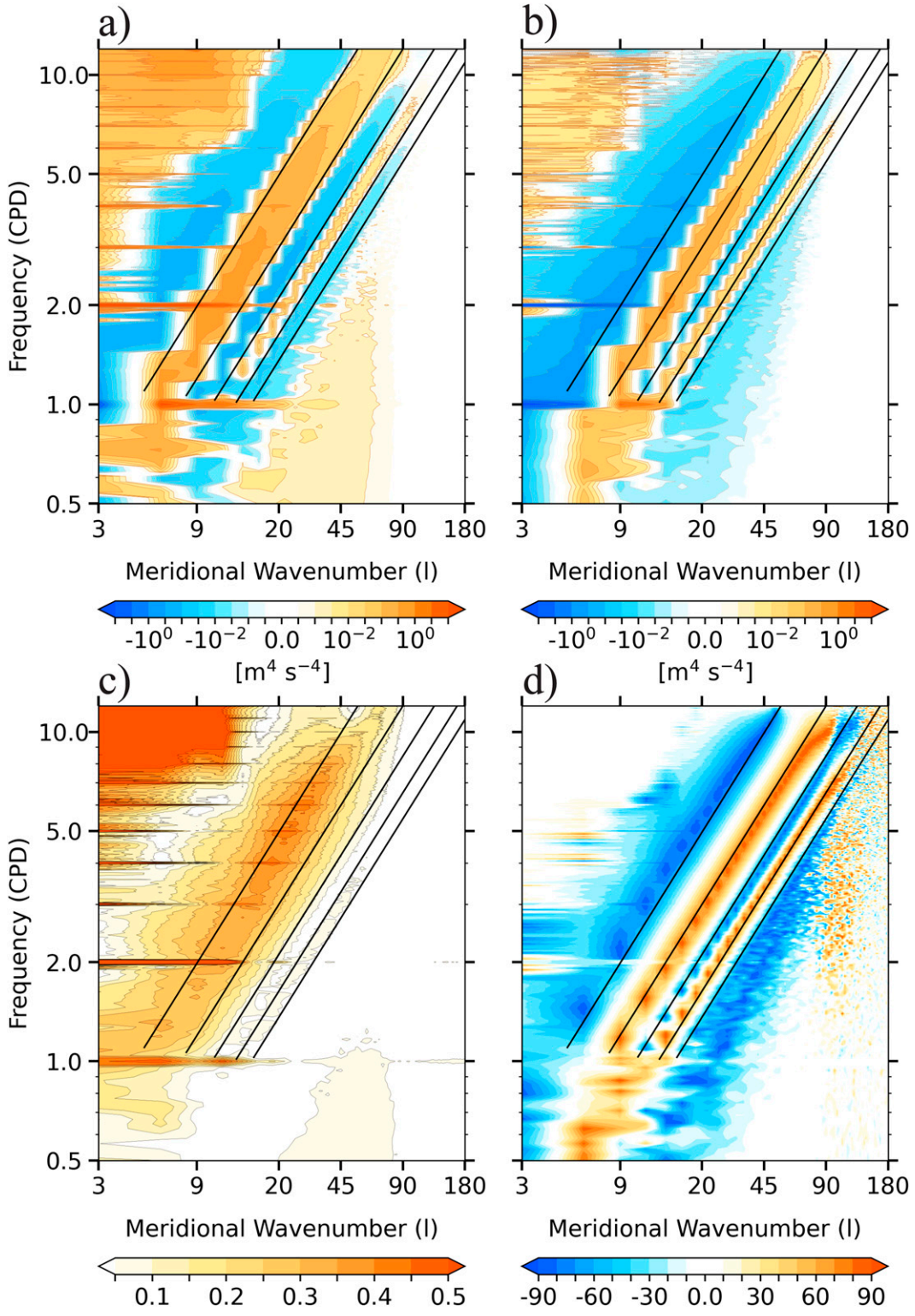

FIG. 16. Meridional wavenumber–frequency (a) cospectrum, (b) quadrature, (c) coherence, and (d) phase spectrum, between geopotential fields at the 10 and 50 hPa levels. The spectra are constructed in the same manner as Fig. 6 except that a Tukey window with $\alpha = 0.33$, which goes to zero at 30°S and 30°N, is applied to each meridian to mitigate the spectral leakage from high wavenumbers. Due to symmetry with respect to $l = 0$, only the northward-propagating waves are shown. The sloping straight black lines correspond to phase speeds of 51, 31, 22, 17, and 14 m s^{-1} from top to bottom, respectively.

variability, which will make them even more valuable for wave-related studies.

Acknowledgments. We thank the anonymous reviewers for their valuable suggestions for improving this paper. This research is supported by the NSF Grant AGS-2202812 and NASA Grant 80NSSC18K1031. The authors declare no conflicts of interest.

Data availability statement. ERA5 hourly data were downloaded from the European Centre for Medium-Range Weather Forecasts (ECMWF), Copernicus Climate Change Service (C3S) at Climate Data Store (CDS; https://cds.climate.copernicus.eu/). The visible image shown in Fig. 1 is from https://www.eorc.jaxa.jp/ptree/index.html. The brightness temperature data shown in Fig. 1 are from http://www.cr.chiba-u.jp/english/database.html.

REFERENCES

Alexander, M. J., and C. Barnet, 2007: Using satellite observations to constrain parameterizations of gravity wave effects for global models. *J. Atmos. Sci.*, **64**, 1652–1665, https://doi.org/10.1175/JAS3897.1.

——, and D. A. Ortland, 2010: Equatorial waves in High Resolution Dynamics Limb Sounder (HIRDLS) data. *J. Geophys. Res.*, **115**, D24111, https://doi.org/10.1029/2010JD014782.

——, J. R. Holton, and D. R. Durran, 1995: The gravity wave response above deep convection in a squall line simulation. *J. Atmos. Sci.*, **52**, 2212–2226, https://doi.org/10.1175/1520-0469(1995)052<2212:TGWRAD>2.0.CO;2.

——, P. T. May, and J. H. Beres, 2004: Gravity waves generated by convection in the Darwin area during the Darwin Area Wave Experiment. *J. Geophys. Res.*, **109**, D20S04, https://doi.org/10.1029/2004JD004729.

——, and Coauthors, 2010: Recent developments in gravity-wave effects in climate models and the global distribution of gravity-wave momentum flux from observations and models. *Quart. J. Roy. Meteor. Soc.*, **136**, 1103–1124, https://doi.org/10.1002/qj.637.

Bretherton, C. S., and P. K. Smolarkiewicz, 1989: Gravity waves, compensating subsidence and detrainment around cumulus clouds. *J. Atmos. Sci.*, **46**, 740–759, https://doi.org/10.1175/1520-0469(1989)046<0740:GWCSAD>2.0.CO;2.

Bushell, A. C., and Coauthors, 2022: Evaluation of the quasi-biennial oscillation in global climate models for the SPARC QBO-initiative. *Quart. J. Roy. Meteor. Soc.*, **148**, 1459–1489, https://doi.org/10.1002/qj.3765.

Butchart, N., J. A. Anstey, Y. Kawatani, S. M. Osprey, J. H. Richter, and T. Wu, 2020: QBO changes in CMIP6 climate projections. *Geophys. Res. Lett.*, **47**, e2019GL086903, https://doi.org/10.1029/2019GL086903.

Corcos, M., A. Hertzog, R. Plougonven, and A. Podglajen, 2021: Observation of gravity waves at the tropical tropopause using superpressure balloons. *J. Geophys. Res. Atmos.*, **126**, e2021JD035165, https://doi.org/10.1029/2021JD035165.

Dee, D. P., and Coauthors, 2011: The ERA-Interim reanalysis: Configuration and performance of the data assimilation system. *Quart. J. Roy. Meteor. Soc.*, **137**, 553–597, https://doi.org/10.1002/qj.828.

Dewan, E. M., and Coauthors, 1998: MSX satellite observations of thunderstorm-generated gravity waves in mid-wave infrared images of the upper stratosphere. *Geophys. Res. Lett.*, **25**, 939–942, https://doi.org/10.1029/98GL00640.

Dunkerton, T. J., 1997: The role of gravity waves in the quasi-biennial oscillation. *J. Geophys. Res.*, **102**, 26 053–26 076, https://doi.org/10.1029/96JD02999.

Ern, M., and Coauthors, 2014: Interaction of gravity waves with the QBO: A satellite perspective. *J. Geophys. Res. Atmos.*, **119**, 2329–2355, https://doi.org/10.1002/2013JD020731.

——, Q. T. Trinh, P. Preusse, J. C. Gille, M. G. Mlynczak, J. M. Russell III, and M. Riese, 2018: GRACILE: A comprehensive climatology of atmospheric gravity wave parameters based on satellite limb soundings. *Earth Syst. Sci. Data*, **10**, 857–892, https://doi.org/10.5194/essd-10-857-2018.

Fritts, D. C., and M. J. Alexander, 2003: Gravity wave dynamics and effects in the middle atmosphere. *Rev. Geophys.*, **41**, 1003, https://doi.org/10.1029/2001RG000106.

Garcia, R. R., and M. L. Salby, 1987: Transient response to localized episodic heating in the tropics. Part II: Far-field behavior. *J. Atmos. Sci.*, **44**, 499–532, https://doi.org/10.1175/1520-0469(1987)044<0499:TRTLEH>2.0.CO;2.

——, A. K. Smith, D. E. Kinnison, Á. de la Cámara, and D. J. Murphy, 2017: Modification of the gravity wave parameterization in the Whole Atmosphere Community Climate Model: Motivation and results. *J. Atmos. Sci.*, **74**, 275–291, https://doi.org/10.1175/JAS-D-16-0104.1.

Geller, M. A., and Coauthors, 2013: A comparison between gravity wave momentum fluxes in observations and climate models. *J. Climate*, **26**, 6383–6405, https://doi.org/10.1175/JCLI-D-12-00545.1.

Gupta, A., T. Birner, A. Dörnbrack, and I. Polichtchouk, 2021: Importance of gravity wave forcing for springtime southern polar vortex breakdown as revealed by ERA5. *Geophys. Res. Lett.*, **48**, e2021GL092762, https://doi.org/10.1029/2021GL092762.

Haertel, P. T., and G. N. Kiladis, 2004: Dynamics of 2-day equatorial waves. *J. Atmos. Sci.*, **61**, 2707–2721, https://doi.org/10.1175/JAS3352.1.

Haiden, T., and Coauthors, 2018: Use of in situ surface observations at ECMWF. ECMWF Tech. Memo. 834, 28 pp., https://doi.org/10.21957/dj9lpy4wa.

Hersbach, H., and Coauthors, 2020: The ERA5 global reanalysis. *Quart. J. Roy. Meteor. Soc.*, **146**, 1999–2049, https://doi.org/10.1002/qj.3803.

Hoffmann, L., and R. Spang, 2022: An assessment of tropopause characteristics of the ERA5 and ERA-Interim meteorological reanalyses. *Atmos. Chem. Phys.*, **22**, 4019–4046, https://doi.org/10.5194/acp-22-4019-2022.

——, and Coauthors, 2019: From ERA-Interim to ERA5: The considerable impact of ECMWF's next-generation reanalysis on Lagrangian transport simulations. *Atmos. Chem. Phys.*, **19**, 3097–3124, https://doi.org/10.5194/acp-19-3097-2019.

Holton, J. R., 1973: An introduction to dynamic meteorology. *Amer. J. Phys.*, **41**, 752–754, https://doi.org/10.1119/1.1987371.

——, J. H. Beres, and X. Zhou, 2002: On the vertical scale of gravity waves excited by localized thermal forcing. *J. Atmos. Sci.*, **59**, 2019–2023, https://doi.org/10.1175/1520-0469(2002)059<2019:OTVSOG>2.0.CO;2.

Jewtoukoff, V., A. Hertzog, R. Plougonven, A. de la Cámara, and F. Lott, 2015: Comparison of gravity waves in the Southern Hemisphere derived from balloon observations and the ECMWF analyses. *J. Atmos. Sci.*, **72**, 3449–3468, https://doi.org/10.1175/JAS-D-14-0324.1.

Kawatani, Y., S. Watanabe, K. Sato, T. J. Dunkerton, S. Miyahara, and M. Takahashi, 2010: The roles of equatorial trapped waves and internal inertia–gravity waves in driving the quasi-biennial oscillation. Part I: Zonal mean wave forcing. *J. Atmos. Sci.*, **67**, 963–980, https://doi.org/10.1175/2009JAS3222.1.

Kim, J.-E., and M. J. Alexander, 2015: Direct impacts of waves on tropical cold point tropopause temperature. *Geophys. Res. Lett.*, **42**, 1584–1592, https://doi.org/10.1002/2014GL062737.

Lane, T. P., and M. W. Moncrieff, 2008: Stratospheric gravity waves generated by multiscale tropical convection. *J. Atmos. Sci.*, **65**, 2598–2614, https://doi.org/10.1175/2007JAS2601.1.

——, M. J. Reeder, and T. L. Clark, 2001: Numerical modeling of gravity wave generation by deep tropical convection. *J. Atmos. Sci.*, **58**, 1249–1274, https://doi.org/10.1175/1520-0469(2001)058<1249:NMOGWG>2.0.CO;2.

Matsuno, T., 1966: Quasi-geostrophic motions in the equatorial area. *J. Meteor. Soc. Japan*, **44**, 25–43, https://doi.org/10.2151/jmsj1965.44.1_25.

Miller, S. D., W. C. Straka, J. Yue, S. M. Smith, M. J. Alexander, L. Hoffmann, M. Setvák, and P. T. Partain, 2015: Upper atmospheric gravity wave details revealed in nightglow satellite imagery. *Proc. Natl. Acad. Sci. USA*, **112**, E6728–E6735, https://doi.org/10.1073/pnas.1508084112.

Nolan, D. S., and J. A. Zhang, 2017: Spiral gravity waves radiating from tropical cyclones. *Geophys. Res. Lett.*, **44**, 3924–3931, https://doi.org/10.1002/2017GL073572.

Pahlavan, H. A., Q. Fu, J. M. Wallace, and G. N. Kiladis, 2021a: Revisiting the quasi-biennial oscillation as seen in ERA5. Part I: Description and momentum budget. *J. Atmos. Sci.*, **78**, 673–691, https://doi.org/10.1175/JAS-D-20-0248.1.

——, J. M. Wallace, Q. Fu, and G. N. Kiladis, 2021b: Revisiting the quasi-biennial oscillation as seen in ERA5. Part II: Evaluation of waves and wave forcing. *J. Atmos. Sci.*, **78**, 693–707, https://doi.org/10.1175/JAS-D-20-0249.1.

Pautet, P.-D., M. J. Taylor, S. D. Eckermann, and N. Criddle, 2019: Regional distribution of mesospheric small-scale gravity waves during DEEPWAVE. *J. Geophys. Res. Atmos.*, **124**, 7069–7081, https://doi.org/10.1029/2019JD030271.

Piani, C., D. Durran, M. J. Alexander, and J. R. Holton, 2000: A numerical study of three-dimensional gravity waves triggered by deep tropical convection and their role in the dynamics of the QBO. *J. Atmos. Sci.*, **57**, 3689–3702, https://doi.org/10.1175/1520-0469(2000)057<3689:ANSOTD>2.0.CO;2.

Podglajen, A., A. Hertzog, R. Plougonven, and B. Legras, 2016: Lagrangian temperature and vertical velocity fluctuations due to gravity waves in the lower stratosphere. *Geophys. Res. Lett.*, **43**, 3543–3553, https://doi.org/10.1002/2016GL068148.

——, ——, ——, and ——, 2020: Lagrangian gravity wave spectra in the lower stratosphere of current (re)analyses. *Atmos. Chem. Phys.*, **20**, 9331–9350, https://doi.org/10.5194/acp-20-9331-2020.

Preusse, P., M. Ern, P. Bechtold, S. D. Eckermann, S. Kalisch, Q. T. Trinh, and M. Riese, 2014: Characteristics of gravity waves resolved by ECMWF. *Atmos. Chem. Phys.*, **14**, 10 483–10 508, https://doi.org/10.5194/acp-14-10483-2014.

Rapp, M., and Coauthors, 2021: SOUTHTRAC-GW: An airborne field campaign to explore gravity wave dynamics at the world's strongest hotspot. *Bull. Amer. Meteor. Soc.*, **102**, E871–E893, https://doi.org/10.1175/BAMS-D-20-0034.1.

Richter, J. H., J. A. Anstey, N. Butchart, Y. Kawatani, G. A. Meehl, S. Osprey, and I. R. Simpson, 2020: Progress in simulating the quasi-biennial oscillation in CMIP models. *J. Geophys. Res. Atmos.*, **125**, e2019JD032362, https://doi.org/10.1029/2019JD032362.

Sakazaki, T., and K. Hamilton, 2020: An array of ringing global free modes discovered in tropical surface pressure data. *J. Atmos. Sci.*, **77**, 2519–2539, https://doi.org/10.1175/JAS-D-20-0053.1.

Schroeder, S., P. Preusse, M. Ern, and M. Riese, 2009: Gravity waves resolved in ECMWF and measured by SABER. *Geophys. Res. Lett.*, **36**, L10805, https://doi.org/10.1029/2008GL037054.

Shepherd, T. G., I. Polichtchouk, R. Hogan, and A. J. Simmons, 2018: Report on Stratosphere Task Force. ECMWF Tech. Memo. 824, 34 pp., https://doi.org/10.21957/0vkp0t1xx.

Skamarock, W. C., S.-H. Park, J. B. Klemp, and C. Snyder, 2014: Atmospheric kinetic energy spectra from global high-resolution nonhydrostatic simulations. *J. Atmos. Sci.*, **71**, 4369–4381, https://doi.org/10.1175/JAS-D-14-0114.1.

Song, I.-S., H.-Y. Chun, and T. P. Lane, 2003: Generation mechanisms of convectively forced internal gravity waves and their propagation to the stratosphere. *J. Atmos. Sci.*, **60**, 1960–1980, https://doi.org/10.1175/1520-0469(2003)060<1960:GMOCFI>2.0.CO;2.

Stephan, C. C., and A. Mariaccia, 2021: The signature of the tropospheric gravity wave background in observed mesoscale motion. *Wea. Climate Dyn.*, **2**, 359–372, https://doi.org/10.5194/wcd-2-359-2021.

Tseng, H.-H., and Q. Fu, 2017: Temperature control of the variability of tropical tropopause layer cirrus clouds. *J. Geophys. Res. Atmos.*, **122**, 11 062–11 075, https://doi.org/10.1002/2017JD027093.

Wallace, J. M., and P. V. Hobbs, 2006: *Atmospheric Science: An Introductory Survey*. Elsevier, 505 pp.

Wheeler, M., and G. N. Kiladis, 1999: Convectively coupled equatorial waves: Analysis of clouds and temperature in the wavenumber–frequency domain. *J. Atmos. Sci.*, **56**, 374–399, https://doi.org/10.1175/1520-0469(1999)056<0374:CCEWAO>2.0.CO;2.

Wright, C. J., N. P. Hindley, M. J. Alexander, L. A. Holt, and L. Hoffmann, 2021: Using vertical phase differences to better resolve 3D gravity wave structure. *Atmos. Meas. Tech.*, **14**, 5873–5886, https://doi.org/10.5194/amt-14-5873-2021.

——, and Coauthors, 2022: Surface-to-space atmospheric waves from Hunga Tonga–Hunga Ha'apai eruption. *Nature*, **609**, 741–746, https://doi.org/10.1038/s41586-022-05012-5.

Yamashita, C., H.-L. Liu, and X. Chu, 2010: Gravity wave variations during the 2009 stratospheric sudden warming as revealed by ECMWF-T799 and observations. *Geophys. Res. Lett.*, **37**, L22806, https://doi.org/10.1029/2010GL045437.